

A Variational Staggered Particle Framework for Incompressible Free-Surface Flows

Xiaowei He, Huamin Wang, Guoping Wang, Hongan Wang and Enhua Wu

Abstract—Smoothed particle hydrodynamics (SPH) has been extensively studied in computer graphics to animate fluids with versatile effects. However, SPH still suffers from two numerical difficulties: the particle deficiency problem, which will deteriorate the simulation accuracy, and the particle clumping problem, which usually leads to poor stability of particle simulations. We propose to solve these two problems by developing an approximate projection method for incompressible free-surface flows under a variational staggered particle framework. After particle discretization, we first categorize all fluid particles into four subsets. Then according to the classification, we propose to solve the particle deficiency problem by analytically imposing free surface boundary conditions on both the Laplacian operator and the source term. To address the particle clumping problem, we propose to extend the Taylor-series consistent pressure gradient model with kernel function correction and semi-analytical boundary conditions. Compared to previous approximate projection method [1], our incompressibility solver is stable under both compressive and tensile stress states, no pressure clumping or iterative density correction (e.g., a density constrained pressure approach) is necessary to stabilize the solver anymore. Motivated by the Helmholtz free energy functional, we additionally introduce an iterative particle shifting algorithm to improve the accuracy. It significantly reduces particle splashes near the free surface. Therefore, high-fidelity simulations of the formation and fragmentation of liquid jets and sheets are obtained for both the two-jets and milk-crown examples.

Index Terms—particle deficiency, nonlocal, smoothed particle hydrodynamics, incompressibility, tensile instability.

1 INTRODUCTION

Due to the meshless, Lagrangian nature, particle methods have been commonly used in computer graphics to animate incompressible free-surface flows. In general, particle methods applied for free-surface flows can be categorized into two families: one is based on an equation of state (EOS), which either uses a non-iterative strategy [2] or an iterative one [3], [4], [5], and the other is based on projection, which either tries to solve a constant density field [6] or a divergence-free velocity field [7]. Although those studies have shown a promising potential of particle methods in creating large-scale splashing fluids, the full exploitation of particle methods in creating subtle effects of fluids is still hampered by numerical problems involving both inaccuracy and instability. One obvious example that is difficult for above mentioned methods to create is the *viscous fingering* effect in the milk splash, as demonstrated in Figure 1.

Two numerical problems that have long plagued particle methods in modeling incompressible free-surface flows are the particle deficiency and the particle clumping problems [8]. The particle deficiency problem is an issue where

only particles inside the boundary contribute to the summation of particle interactions for particles near the free-surface boundary. The missing particles usually will have a negative impact on simulation accuracy [9]. Furthermore, since we only store a finite and often small number of particle neighbors in real implementation, the particle deficiency problem can also arise for interior particles when the particle distribution becomes irregular during the simulation [10]. The particle clumping problem is a situation where particles may unnaturally cluster together resulted from a combined action of stress states and kernel functions [11]. For some historical reasons, the particle clumping problem arising from a tensile stress state is usually referred to as tensile instability [12], [13] while that arising from a compressive stress state referred to as pairing instability [14], [15]. Nevertheless, some researchers in engineering do not make an explicit distinction between tensile instability and pairing instability, e.g., Sugiura and Inutsuka [16] refer to both instabilities as the tensile instability. Since there is no naming unification for the particle clumping problem yet and the term ‘tensile’ is sometimes misleading, we will use the term tensile instability specifically for the particle clumping problem arising from negative stress regimes and pairing instability for the particle clumping problem arising from positive stress regimes in the following discussion. A sufficient condition for checking unstable growth of tensile instability in terms of the stress state and the second derivative of smoothing function was first proposed by Swegle et al. [12]. However, Dehnen and Aly [15] later disproved their statement by pointing out that the Wendland kernels does not suffer from the pairing instability despite having vanishing derivative at the origin. To avoid the particle clumping problem, researchers in computer graphics have

• X. He is with the State Key Lab. of CS, Institute of Software, Chinese Academy of Sciences.
E-mail: xiaowei@iscas.ac.cn

• H. Wang is with the Ohio State University.
E-mail: whmin@cse.ohio-state.edu

• G. Wang is with the Peking University.
E-mail: wgp@pku.edu.cn

• H. Wang is with Institute of Software, Chinese Academy of Sciences.
E-mail: hongan@iscas.ac.cn

• E. Wu is with Institute of Software, Chinese Academy of Sciences and the University of Macau.
E-mail: ehwu@umac.mo



Fig. 1. A photograph capturing the milk crown with viscous fingering structures resulted from the interaction among pressure, viscosity and surface tension.

either clamped negative pressures to zero [6], [7] or added an artificial pressure [17] to remove cohesive forces. Unfortunately, the cohesive force imposed on boundary particles, which are the key to create the viscous fingering effect, will also be removed. According to Belytschko and Xiao [18], perfect elimination of tensile instability appears to be unachievable as long as an Eulerian kernel is used with a purely Lagrangian description of motion. Nevertheless, it is possible for us to minimize the influence of tensile instability by improving the accuracy of particle methods, e.g., by resolving the particle deficiency problem as mentioned earlier or selecting an appropriate kernel function.

Motivated by the variational framework [19] and recent developments on nonlocal methods [1], [20], [21], we first reformulate incompressible free-surface flows as an energy minimization problem under a variational staggered particle framework. Although the equivalence between solving a pressure Poisson equation and an energy minimization problem can be easily established for a uniform-grid based discretization, their equivalence is not quite obvious for a particle discretization. To get a stable and accurate simulation based on particles, both the discretized pressure Poisson equation and the pressure forces should be derived by meticulously addressing the particle deficiency and particle clumping problems. During the derivation, we have made the following contributions

- A reformulation of the particle discretized pressure Poisson equation derived from a variational staggered particle framework for incompressible free-surface flows.
- A new semi-analytic strategy to impose free-surface boundary conditions on both the Laplacian operator and the source term.
- An extended Taylor-series consistent pressure gradient model that is stable under both compressive and tensile stress states.
- An iterative particle shifting algorithm motivated by the Helmholtz free energy functional that not only helps regularize particle distributions, but also capture realistic surface tension effects.



Fig. 2. A milk crown generated by our method and realistic fingering structures can be noticed around the rim of the milk crown.

2 RELATED WORK

Since SPH was first invented by Lucy [22] and Gingold and Monaghan [23], various techniques have been proposed to solve the fluid incompressibility.

EOS-based methods. Before SPH was first introduced into computer graphics by Desbrun and Gascuel [24], it had been applied in engineering to solve a wide range of dynamical problems (please see [25] for a review). Researchers in computer graphics initially applied an equation of state (EOS) based on either a gas equation [26] or Tait's equation [27] to model weakly compressible fluids. To remove time step restrictions, Solenthaler and Pajarola [3] proposed a predictive-corrective incompressible SPH (PCISPH) to correct the density error iteratively. Their method can handle time steps which are up to two orders of magnitude larger than previous non-iterative EOS-based methods. He and colleagues [4] pointed out that the convergence rate of an iterative method is closely related to a particle's influence domain and proposed a local Poisson SPH (LSPSH) method to solve the incompressibility. Bodin et al. [28] enforced the incompressibility by solving a system of velocity constraints. Recently, Macklin and Müller [5] presented an iterative density solver based on position based dynamics, which showed a better stability and performance than previous iterative methods. For a thorough review, we refer to the work [29]. In case readers are interested in recent progress of SPH in engineering, please refer to other review papers [11], [30].

Projection-based methods. In solving the pressure Poisson equation, both the Laplacian operator and the source term should be discretized. According to [31], the most commonly used way to discretize the PPE in SPH is the finite difference scheme introduce by [32], which is usually referred to as the approximate projection method. Along this direction, Shao et al [33] presented an ISPH method to simulate Newtonian and non-Newtonian flows with free surfaces. He et al. [1] proposed an approximate projection method based on staggered particles to solve the zero-energy mode problem, but leaves the particle deficiency problem untouched. Nair and Gaurav [34] presented a semi-analytical approach to impose a zero pressure boundary condition on free surfaces, achieving to an improved Lapla-

cian operator for the pressure Poisson equation. Yang et al. [35] further improved the accuracy by considering the particle deficiency for the pressure force formulation.

Other methods use the double summation scheme for discretization, which can be referred to as the exact projection method. Hu and Adams [36] proposed to correct intermediate density errors by adjusting the half-time-step velocity with exact projection for incompressible multi-phase SPH. Ihmsen et al. [6] presented an implicit incompressible SPH (IISPH) to unilaterally enforce the incompressibility. Compared to the approximate projection method, the exact projection method is typically regarded as less stable, e.g., it can suffer from oscillations and zero-energy mode if negative particle pressures are not clamped to zero [32]. Later, Bender and Koschier [7] improved the IISPH method by iteratively enforcing the divergence-free condition. Band et al. [37] improved the solid wall boundary condition for IISPH. Cornelis et al [38] presented an analysis of two source terms and proposed to incorporate velocity divergence and particle shift to reduce artificial viscosity.

Alternatively, the pressure Poisson equation can be solved on a regular grid [39], [40] with a similar idea to FLIP [41], but at a cost of losing the purely Lagrangian nature of SPH. For more details about recent developments on projection-based particle methods in engineering, please refer to the work [8].

Inherent numerical problems. The development of projection-based SPH methods in computer graphics is much slower than the EOS-based methods. The reason is that the pressure Poisson equation is sensitive to the underlying particle distribution and suffers from numerical problems involving particle deficiency and tensile instability. For a truly incompressible fluid, the negative pressures should not be simply removed. Therefore, a robust and accurate fluid solver for incompressible free-surface flows is required. To our best knowledge, only little work has been done in computer graphics on how to solve the above mentioned numerical problems. Schechter and Bridson [42] added ghost air particles to help resolve the particle deficiency problem, but it requires a significant extra computational cost. Macklin and Müller [5] and He et al [17] added an artificial pressure to alleviate the tensile instability, which is equivalent to adding an artificial surface tension or removing negative pressures, respectively. However, none of these techniques work well for the projection methods. In engineering, the numerical problems have also been extensively studied [8]. However, as pointed out in their work, both the stability and accuracy of particle methods have not yet fully addressed.

3 A VARIATIONAL STAGGERED PARTICLE FRAMEWORK

In the context of projection-based methods, the incompressibility of a free-surface flow is enforced by solving the following pressure Poisson equation

$$\nabla \cdot \left(\frac{\Delta t}{\rho} \nabla p \right) = \nabla \cdot \mathbf{v}^*, \quad \text{inside } \Omega, \quad (1)$$

$$p = 0, \quad \text{on } \partial\Omega,$$

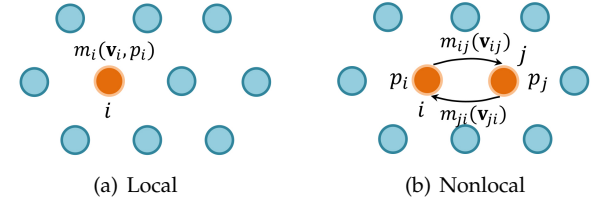


Fig. 3. Local vs nonlocal variational frameworks. (a) Under a local variational framework, all physical quantities are carried on the same particles; (b) Under our variational staggered particle framework, particle masses and velocities are decoupled from original particles and defined as nonlocal variables.

where Ω is the fluid region with free surface boundary $\partial\Omega$, p is the pressure, Δt is the time step, ρ is the density and \mathbf{v}^* represents the intermediate velocity which has considered all forces except the pressure force.

3.1 Motivation

According to [19], the pressure Poisson equation can be reformulated as an energy minimization problem

$$\min_p \int_{\Omega} \frac{1}{2} \rho \left\| \mathbf{v}^* - \frac{\Delta t}{\rho} \nabla p \right\|^2 dV, \quad p = 0 \text{ on } \partial\Omega. \quad (2)$$

Intuitively speaking, enforcing a fully incompressible fluid is equivalent to maximally dissipating the kinetic energy by using the pressure force. The question is how can we formulate the energy minimization problem in SPH?

Figure 3a demonstrates the standard discretization for a fluid region in SPH, where each particle i carries a set of local physical quantities including the particle mass m_i , velocity \mathbf{v}_i and pressure p_i , etc. We call the quantities to be *local* because their values only depend on the position of particle i . In this sense, the pressure gradient ∇p estimated in traditional SPH is also a local quantity. Inserting all local quantities into Equation 2, a local form of discretization for the energy minimization problem can be derived as

$$\min_p \sum_{i,j} \frac{1}{2} m_i \left\| \mathbf{v}_i^* - \frac{\Delta t}{\rho_0} \sum_j \frac{m_j}{\rho_j} \left(\frac{p_i + p_j}{2} \right) \nabla_i W \right\|^2, \quad (3)$$

where p_i is zero for air boundary particles, W is the kernel function, ρ_0 is the reference density, j represents all neighbors of particle i . Taking the derivative of Equation 3 with respect to p_i , we obtain a discretized pressure Poisson equation that corresponds to an exact projection where the second-ring neighbors of particle i 's neighbors should also be taken into account for projection. As pointed in [32], the major problem with the exact SPH projection method is that it suffers from the spurious zero-energy mode problem, which means the pressure field could be oscillating unnaturally. The underlying reason is that both the pressure and velocity are local variables and defined at the same location. He and his colleagues [1] propose to address the zero-energy mode problem by introducing staggered particles. The core idea of their method is to decouple the definition of the pressure and other physical quantities and define their values at different locations. This inspires us to introduce nonlocal quantities and reformulate the energy minimization problem in Equation 2 to be a staggered form in the following section.

3.2 Our Discretization

Before deriving the variational staggered particle framework, we introduce two types of functions first: point functions that refer to functions defined on single particles and two-point functions that refer to functions defined for pairs of particles, e.g., we define $\psi(\mathbf{x}_i)$ as local scalars and $\psi(\mathbf{x}_i, \mathbf{x}_j)$ as nonlocal scalars. We refer to the work of Du et al [20] for more details on the discussion of nonlocal operators. Figure 3b demonstrates a staggered discretization strategy that both the mass and velocity are defined as two-point functions

$$m_{ij} = \underline{m}(\mathbf{x}_i, \mathbf{x}_j), \quad \mathbf{v}_{ij} = \underline{\mathbf{v}}(\mathbf{x}_i, \mathbf{x}_j), \quad (4)$$

where the underline is used to distinguish two-point functions from point functions. Besides, we assume the pressure force imposed on m_{ij} is only related to particle i and j , as was done in [1], the pressure gradient imposed on m_{ij} is expressed as follows

$$\nabla_{ij} p = \frac{p_j - p_i}{r_{ij}} \mathbf{n}_{ij}, \quad (5)$$

in which $r_{ij} = \|\mathbf{x}_j - \mathbf{x}_i\|$ and $\mathbf{n}_{ij} = (\mathbf{x}_j - \mathbf{x}_i) / r_{ij}$. Inserting both Equation 4 and 5 into Equation 2, we get the following staggered formulation of the energy minimization problem

$$\min_p \sum_{i,j} \frac{1}{2} m_{ij} \left\| \mathbf{v}_{ij}^* - \frac{\Delta t}{\rho_0} \left(\frac{p_j - p_i}{r_{ij}} \right) \mathbf{n}_{ij} \right\|^2. \quad (6)$$

The major difference between Equation 6 and 3 is that the pressure and velocity field are decoupled in equation 6, which is the key to solve the zero-energy mode problem.

Now we discuss how to calculate the nonlocal mass m_{ij} and velocity \mathbf{v}_{ij} . Assume the particle mass and velocity are initially stored as local variables m_i and \mathbf{v}_i , we introduce the following two-point operators to map local variables to nonlocal ones

$$m_{ij} = \frac{\omega_{ij}}{\alpha_i} m_i, \quad \mathbf{v}_{ij} = \frac{\mathbf{v}_i + \mathbf{v}_j}{2}, \quad (7)$$

where ω_{ij} is a weighting function required to be symmetric, i.e., $\underline{\omega}(\mathbf{x}_i, \mathbf{x}_j) = \underline{\omega}(\mathbf{x}_j, \mathbf{x}_i)$. By temporarily ignoring the particle deficiency problem, we are able to define the value of α_i to be $\alpha_i = \sum_j \omega_{ij}$, where the total mass and momentum can be verified to be conservative after the mapping. Note that the masses m_{ij} and m_{ji} may not be equal due to irregular particle distributions. After inserting Equation 7 into Equation 6, we get the following discretized pressure Poisson equation by taking the derivative with respect to p_i

$$\begin{aligned} & \sum_j \frac{1}{\rho_0} \left(\frac{1}{\alpha_i} + \frac{1}{\alpha_j} \right) \frac{p_i - p_j}{r_{ij}^2} \omega_{ij} \\ &= \frac{1}{\Delta t} \sum_j \left(\frac{1}{\alpha_i} + \frac{1}{\alpha_j} \right) \left(\frac{\mathbf{v}_i^* + \mathbf{v}_j^*}{2} \right) \cdot \frac{\mathbf{n}_{ij}}{r_{ij}} \omega_{ij}, \end{aligned} \quad (8)$$

in which we have assumed all particles carry equal masses. The left-hand side of Equation 8 now represents an approximate Laplacian operator while the right-hand side represents a source term. More details on how to correct the value of α_i as well as the discretized pressure Poisson

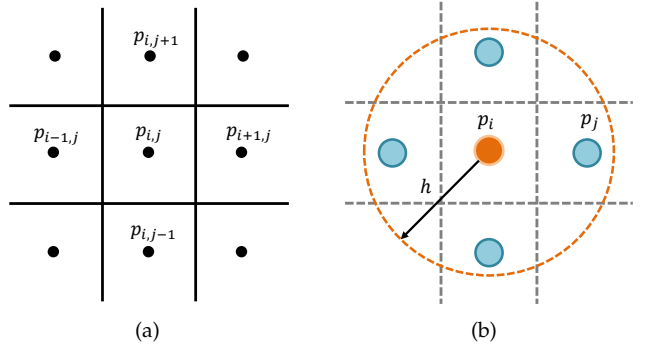


Fig. 4. (a) The two-dimensional MAC grid, (b) An uniform particle distribution with four neighbors. The particle-based Laplacian operator proposed by [Cummins and Rudman 1999] is identical to the grid-based Laplacian operator only when we pick an exponential function, e.g., $W = e^{-\ln r}$, to be the kernel function.

equation to account for the particle deficiency problem will be later discussed in section 4.

Comparison to [Cummins and Rudman 1999]. The Laplacian operator proposed by Cummins and Rudman [32] is defined as

$$\sum_j \frac{m_j}{\rho_j} \left(\frac{4}{\rho_i + \rho_j} \right) \frac{p_i - p_j}{r_{ij}^2} (\mathbf{x}_i - \mathbf{x}_j) \cdot \nabla_i W_{ij}. \quad (9)$$

In case the fluid is ideally incompressible, we can verify that Equation 9 is equal to the left hand side of Equation 8 only if we impose the following two constraints

$$W_{ij} = \omega_{ij} = -r_{ij} \frac{\partial W_{ij}}{\partial r_{ij}}. \quad (10)$$

$$\rho_i = \rho_0 = \sum_j m_j W_{ij}. \quad (11)$$

To satisfy the condition in Equation 10, the kernel function W should be in the form of an exponential function, i.e., $W_{ij} = e^{-\ln r_{ij}}$. Unfortunately, an exponential function is usually not a good kernel function for the projection-based methods, because the value of $(p_i - p_j)/r_{ij}^2$ can become too large if a neighbor j is close to particle i , and thus may cause instabilities during the simulation. Therefore, in traditional SPH methods, it is common to use kernel functions whose gradient is zero at the original point where the values of W_{ij} and $-\partial W_{ij}/\partial r_{ij}$ are usually different. Therefore, we need to meticulously calculate the pressure force to avoid tensile instabilities under compressive stress states [43], especially when the Laplacian and gradient operator are discretized in different ways [44]. Among all discretization strategies, it is really hard to tell which pair of the Laplacian and gradient operators is the best to solve the pressure Poisson equation. In fact, we can actually notice from Figure 4 that the particle-based Laplacian operator defined in Equation 9 does not even converge to an grid-based Laplacian operator if we choose an arbitrary kernel function. Nevertheless, our discretization formulation does not suffer the above mentioned problems as both the Laplacian and gradient operators are derived uniformly under the same variational staggered particle framework. Later, we will show how to resolve the particle clumping problem in section 5 by selecting the

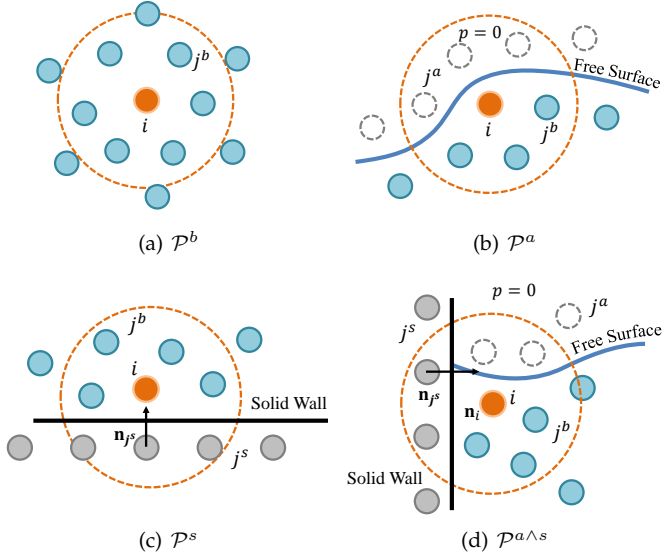


Fig. 5. Illustration for our principle in categorizing all fluid particles into four subsets based on the intersection testing between a particle's support domain and fluid boundaries.

right kernel function and introducing a correction for the kernel function, therefore no adhoc tricks, e.g., the dynamic stabilization [43], are required to stabilize the PPE solver any more.

4 SOLVING THE PARTICLE DEFICIENCY PROBLEM

In this section, we will discuss how to address the particle deficiency problem for each part of Equation 8. In our implementation, ghost solid particles are uniformly seeded near the solid wall within a distance that equals to the smoothing length h at the beginning of simulation. Since dynamic creation of ghost air particles is time consuming, we propose a semi-implicit method, motivated by [17], [34], to virtually account for the contribution from ghost air particles. To facilitate the following discussion, let us first assume that ghost air particles still exist, and denote ghost air neighbors as $j^a \in \mathcal{N}_i^a$, ghost solid neighbors as $j^s \in \mathcal{N}_i^s$ and fluid neighbors as $j^b \in \mathcal{N}_i^b$, thus we have $\mathcal{N}_i = \mathcal{N}_i^a \cup \mathcal{N}_i^b \cup \mathcal{N}_i^s$.

4.1 Correcting the Laplacian operator

Following the derivation of Bridson [45], if a particle neighbor j^a is a ghost air particle, we can set p_{j^a} in Equation 8 simply to be zero. Otherwise, if a particle neighbor j^s is a ghost solid particle, the velocity change $\Delta\mathbf{v}_{ij^s}^*$ of the staggered particle m_{ij^s} caused by pressure force can be expressed as

$$\Delta\mathbf{v}_{ij^s}^* = -\frac{\Delta t}{\rho_0} \nabla_{ij^s} p, \quad (12)$$

where $\nabla_{ij^s} p$ is the pressure gradient defined in Equation 5. However, to flexibly control the slipperiness of the solid wall boundary, it can be noticed that the velocity change $\Delta\mathbf{v}_{ij^s}^*$ can also be defined as the following constraint [1]

$$\begin{aligned} \Delta\mathbf{v}_{ij^s}^* &= c^n \text{proj}_{\mathbf{n}_{j^s}} (\mathbf{v}_{j^s} - \mathbf{v}_i^*) \\ &+ c^t \left[(\mathbf{v}_{j^s} - \mathbf{v}_i^*) - \text{proj}_{\mathbf{n}_{j^s}} (\mathbf{v}_{j^s} - \mathbf{v}_i^*) \right], \end{aligned} \quad (13)$$

where \mathbf{v}_{j^s} represents the velocity of the ghost solid neighbor j^s , \mathbf{n}_{j^s} is a normal vector calculated from the signed distance field of the solid wall boundary, $\text{proj}_{\mathbf{n}_{j^s}} (\mathbf{v}_{j^s} - \mathbf{v}_i^*)$ represents the projection of $\mathbf{v}_{j^s} - \mathbf{v}_i^*$ on \mathbf{n}_{j^s} , c^n and c^t are two independent constants in the range of $[0, 1]$ to control the solid wall boundary condition. Intuitively speaking, c^t controls the sliding speed between particle i and j^s . Therefore, the value of c^t can be set to 1 for a no-slip boundary condition and 0 for a free-slip boundary condition. c^n controls the normal speed between particle i and j^s . To prevent particle i from interpenetrating into the solid wall, we will always set c^n to 1 when particle i approaches particle j^s (i.e., $(\mathbf{v}_{j^s} - \mathbf{v}_i^*) \cdot \mathbf{n}_{j^s} > 0$). Otherwise, we can control the strength of the fluid stickiness to the wall by adjusting the value of c^n .

After inserting all boundary conditions (please refer to Appendix for the whole derivation), the Laplacian operator in Equation 8 can be reformulated as follows

$$\mathcal{L}_i = \frac{\hat{A}_i}{\rho_0} p_i - \frac{1}{\rho_0} \sum_{j^b} \left(\frac{1}{\hat{\alpha}_i} + \frac{1}{\hat{\alpha}_j} \right) \frac{\omega_{ij}}{r_{ij}^2} p_j, \quad (14)$$

where

$$\hat{A}_i = \sum_{j^a \cup j^b} \left(\frac{1}{\hat{\alpha}_i} + \frac{1}{\hat{\alpha}_j} \right) \frac{\omega_{ij}}{r_{ij}^2} \quad (15)$$

and $\hat{\alpha}_i = \sum_j \omega_{ij}$ represents the total weight of a fluid particle with full neighbors. The question is how can we calculate $\hat{\alpha}_i$ and \hat{A}_i without knowing the locations of all ghost air particles in advance?

To avoid creating all ghost air particles j^a , we precompute two thresholds α_0 and A_0 for an interior prototype particle with full fluid neighbors at the beginning of simulation as follows

$$\alpha_0 = \sum_j \omega_{ij}, \quad A_0 = \sum_j \left(\frac{1}{\alpha_i} + \frac{1}{\alpha_j} \right) \frac{\omega_{ij}}{r_{ij}^2} \quad (16)$$

In calculating $\hat{\alpha}_i$, we first compute the total weight by only considering contributions from neighbor particles j^b and j^s , i.e., $\alpha_i^{b\wedge s} = \sum_{j^b \cup j^s} \omega_{ij}$. Then, we calculate $\hat{\alpha}_i$ as follows

$$\hat{\alpha}_i = \max(\alpha_0, \alpha_i^{b\wedge s}) \quad (17)$$

to compensate for missing ghost air particles. Equation 17 also indicates that the value of $\alpha_i^{b\wedge s}$ could be occasionally larger than α_0 during the simulation. In that case, $\hat{\alpha}_i$ just equals to $\alpha_i^{b\wedge s}$. Similarly, in calculating \hat{A}_i , we first calculate two terms from neighbors j^b and j^s , which are expressed as

$$A_i^b = \sum_{j^b} \left(\frac{1}{\hat{\alpha}_i} + \frac{1}{\hat{\alpha}_j} \right) \frac{\omega_{ij}}{r_{ij}^2}, \quad A_i^s = \sum_{j^s} \left(\frac{1}{\hat{\alpha}_i} + \frac{1}{\hat{\alpha}_j} \right) \frac{\omega_{ij}}{r_{ij}^2}. \quad (18)$$

Before estimating the contribution from ghost air particles, we categorize all fluid particles into four subsets, as illustrated in Figure 5:

- 1) \mathcal{P}^b : all interior particles whose support domain does not intersect with any of the boundaries, i.e., $\mathcal{N}_i^s = \emptyset$ and $A_i^b \geq A_0$.
- 2) \mathcal{P}^a : all boundary particles whose support domain are only truncated by the free surface boundary, i.e., $\mathcal{N}_i^s = \emptyset$ and $A_i^b < A_0$;

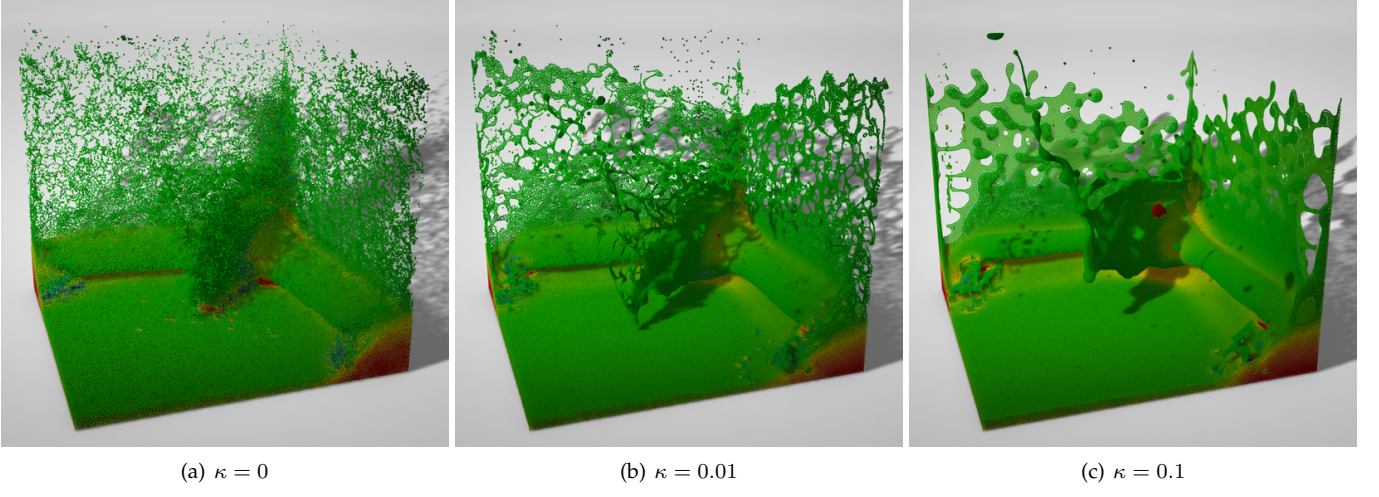


Fig. 6. A three-dimensional dambreak case. This example shows the flow patterns of using different squared gradient energy coefficients.

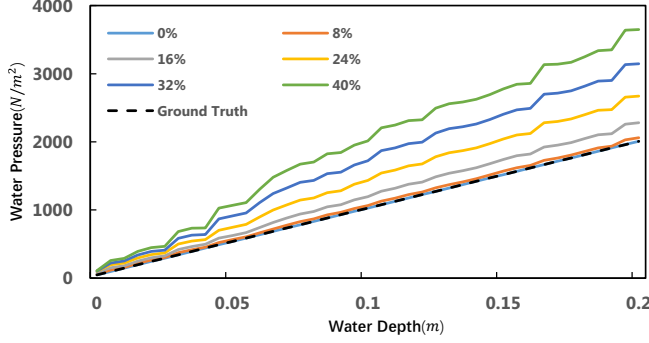


Fig. 7. A hydrostatic water test solved on a uniformly distributed particles with four neighbors. By introducing a random particle shifting, whose maximum magnitude is εd_0 , to the position field, the simulation accuracy largely decreases as the value of ε increases from 0% to 40%.

- 3) \mathcal{P}^s : all boundary particles whose support domain are only truncated by the solid wall boundary, i.e., $\mathcal{N}_i^s \neq \emptyset$ and $A_i^b + A_i^s \geq A_0$;
- 4) $\mathcal{P}^{a \wedge s}$: all boundary particles whose support domain are both truncated by the free surface and solid wall boundaries, i.e., $\mathcal{N}_i^s \neq \emptyset$ and $A_i^b + A_i^s < A_0$;

By invoking the definition of \hat{A}_i in Equation 15, we finally have

$$\hat{A}_i = \begin{cases} A_0, & i \in \mathcal{P}^a \\ A_i^b, & i \in \mathcal{P}^b \cup \mathcal{P}^s \\ A_0 - A_i^s, & i \in \mathcal{P}^{a \wedge s} \end{cases}. \quad (19)$$

Note that ghost air particles are no longer required in calculating \hat{A}_i .

4.2 Correcting the source term

If the particle distribution is regular enough, the following condition should be satisfied for all particles

$$\mathcal{C}_i = \frac{1}{\hat{A}_i} \sum_j \frac{\mathbf{n}_{ij}}{r_{ij}} \omega_{ij} = 0. \quad (20)$$

By invoking the relationship $\hat{\alpha}_i = \hat{\alpha}_j$ for a regular particle distribution, an equivalent relationship is obtained as follows

$$\sum_j \left(\frac{1}{\hat{\alpha}_i} + \frac{1}{\hat{\alpha}_j} \right) \mathbf{v}_i^* \cdot \frac{\mathbf{n}_{ij}}{r_{ij}} \omega_{ij} = 0. \quad (21)$$

Subtracting Equation 21 from the right hand side of Equation 8, the source term becomes

$$\mathcal{D}_i = \frac{1}{\Delta t} \sum_j \left(\frac{1}{\hat{\alpha}_i} + \frac{1}{\hat{\alpha}_j} \right) \left(\frac{\mathbf{v}_j^* - \mathbf{v}_i^*}{2} \right) \cdot \frac{\mathbf{n}_{ij}}{r_{ij}} \omega_{ij} \quad (22)$$

The advantage of applying Equation 22 to compute the divergence of velocity is that this new formulation guarantees a zeroth-order accuracy for arbitrary particle distributions while the previous one will fail to correctly compute the divergence for a constant velocity field. To integrate boundary conditions for \mathcal{D}_i , we assume the velocity of ghost air neighbors is equal to \mathbf{v}_i . By additionally invoking the solid wall boundary condition defined in Equation 13 and assume $\hat{\alpha}_{j^s} = \hat{\alpha}_i$, the source term \mathcal{D}_i for all fluid particles can be expressed as

$$\mathcal{D}_i = \frac{1}{\Delta t} \sum_{j^b} \left(\frac{1}{\hat{\alpha}_i} + \frac{1}{\hat{\alpha}_j} \right) \left(\frac{\mathbf{v}_j^* - \mathbf{v}_i^*}{2} \right) \cdot \mathbf{n}_{ij} \frac{\omega_{ij}}{r_{ij}} + \frac{1}{\Delta t} \begin{cases} 0, & i \in \mathcal{P}^a \cup \mathcal{P}^b \\ \sum_{j^s} \frac{2\Delta\mathbf{v}_{ij}^*}{\hat{\alpha}_i} \cdot \mathbf{n}_{ij} \frac{\omega_{ij}}{r_{ij}}, & i \in \mathcal{P}^s \cup \mathcal{P}^{a \wedge s} \end{cases}. \quad (23)$$

4.3 Particle Shifting

The condition in Equation 20 will be destroyed when particles move anisotropically. To investigate how an irregular particle distribution can affect the fluid evolution, let us consider solving a hydrostatic water test on uniformly distributed particles where only four nearest particles are stored as neighbors. We then introduce a random shift $\delta\mathbf{x}_i$, whose maximum shifting distance is defined as εd_0 , to the position field. By setting ε to different values, a set of pressure fields at $t = 0$ can be solved and plotted at

Figure 7. From the comparison, it can be noted that the simulation accuracy significantly decreases as the magnitude of random particle shifting increases. Therefore, it is necessary to maintain the regularity of particle distribution with particle shifting. Motivated by the finite particle volume method [46], Xu et al. [47] first applied a particle shifting algorithm to avoid non-uniform particle distributions in ISPH, yet it suffers from instabilities for flows near the free surface. Later works [48], [49] have stabilized the particle shifting algorithm by proposing to govern the magnitude and direction of the position shift according to Fick's law. The idea is to shift particles' positions slightly from regions of high particle concentration to regions of low concentration. However, it still results in numerical inconsistencies probably due to inaccuracies in calculation of normal vectors at free-surface and implementation of inconsistent particle shifting displacement equations [50]. Since flows near free-surface are usually related to surface tension effects, we are motivated to combine the particle shifting with some kind of surface tension model to form a new particle shifting algorithm that can both regularize particle distributions and capture surface tension effects.

Inspired by the Helmholtz free energy functional [17], [51], [52], we propose a new particle shifting algorithm that minimizes the following energy

$$\mathcal{F}_i = \frac{1}{2} \frac{\|\mathbf{x}_i - \mathbf{x}_i^*\|^2}{d_0^2} + f(c_i) + \frac{\kappa}{2} \|\nabla_i c\|^2 \quad (24)$$

by treating all particles as having a volume of 1, where c is the concentration variable, d_0 is the sampling distance, κ is a squared gradient energy coefficient. The first term $\frac{1}{2} \|\mathbf{x}_i - \mathbf{x}_i^*\|^2 / d_0^2$ can be viewed as a momentum potential [53], which is included to guarantee the particle movement is as small as possible. The second term $f(c_i)$ represents the bulk energy density, which guarantees the total volume is preserved. Its exact formulation is defined as

$$f(c_i) = \frac{\lambda}{4} \left(\frac{c_i^2}{c_0^2} - 1 \right)^2, \quad (25)$$

where λ is the bulk energy coefficient and c_0 is a reference value for c_i . By taking a weighting function $W(r)$ that meets $dW/dr = \omega/r$ and defining c_i as

$$c_i = \frac{1}{\hat{\alpha}_i} \sum_j W_{ij}, \quad (26)$$

we can finally compute $\nabla_i c$ as

$$\nabla_i c = \frac{1}{\hat{\alpha}_i} \sum_j \frac{\mathbf{n}_{ij}}{r_{ij}} \omega_{ij}. \quad (27)$$

Minimizing the squared gradient energy density is equivalent to imposing the condition in Equation 20 for interior particles. The advantage of transferring Equation 20 into the energy minimization problem is that the squared gradient energy enables us to capture the correct surface tension effects for boundary particles as well [17].

To solve the optimization problem, we apply a strategy based on Ficks law of diffusion to regularize the particle distribution iteratively [48]. Its purpose is to shift particles from regions of high Helmholtz free energy concentration to

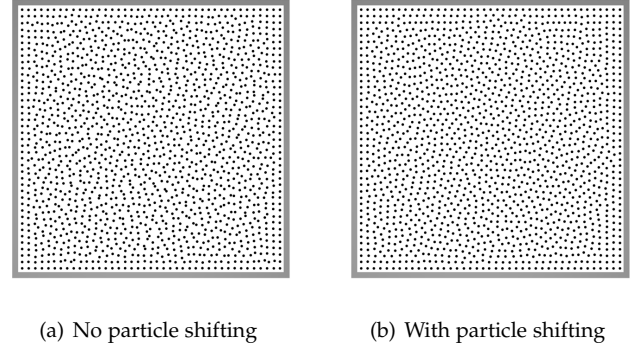


Fig. 8. Particle distributions in a Taylor-Green vortex at $t = 0.4s$.

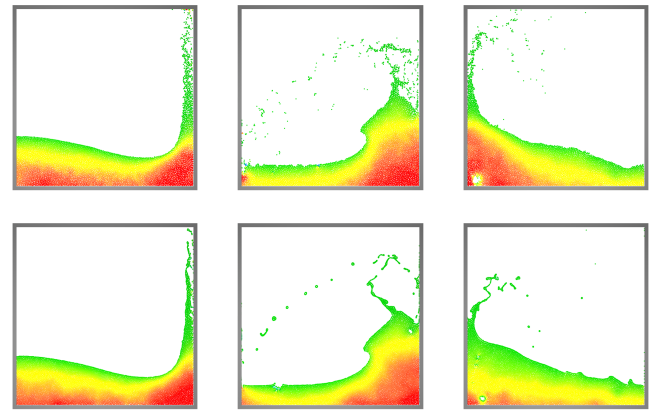


Fig. 9. Side by side comparison of a two-dimensional dam-break example between taking a particle shifting algorithm with surface tension effects (Bottom) and without taking the particle shifting (Top).

regions of low concentration. At each iteration, the displacement vector for particle i is written as

$$\delta\mathbf{x}_i = -\varsigma \nabla_i \mathcal{F} \quad (28)$$

where $\nabla_i \mathcal{F}$ is computed by taking the derivative of \mathcal{F}_i with respect to \mathbf{x}_i

$$\nabla_i \mathcal{F} = \frac{\mathbf{x}_i - \mathbf{x}_i^*}{d_0^2} + \lambda \left(\frac{c_i^3}{c_0^4} - \frac{c_i}{c_0^4} \right) \nabla_i c + \kappa (\Delta_i c) \nabla_i c. \quad (29)$$

Here $\Delta_i c$ is defined as

$$\Delta_i c = \frac{1}{\hat{\alpha}_i} \sum_j \frac{\omega'_{ij}}{r_{ij}}. \quad (30)$$

ς is a coefficient that controls the distance a particle moves during one iteration. By noting that

$$\begin{aligned} \|\nabla_i \mathcal{F}\| &\leq \left\| \frac{\mathbf{x}_i - \mathbf{x}_i^*}{d_0^2} \right\| + \lambda \left\| \left(\frac{c_i^3}{c_0^4} - \frac{c_i}{c_0^4} \right) \nabla_i c \right\| + \kappa \|(\Delta_i c) \nabla_i c\| \\ &\leq \frac{1}{d_0} + \frac{\lambda_0}{c_0} + \kappa_0 (\Delta_0 c), \end{aligned} \quad (31)$$

where $\Delta_0 c$ is a reference value for $\Delta_i c$, λ_0 and κ_0 are the upper limits for λ and κ which are simply set to 1, we define the coefficient ς to be as

$$\varsigma = d_0 \sqrt{\left[\frac{1}{d_0} + \frac{\lambda_0}{c_0} + \kappa_0 (\Delta_0 c) \right]}. \quad (32)$$

Therefore, an upper limit of d_0 is imposed on the particle shifting distance for one iteration.

Figure 8 demonstrates the effectiveness of our particle shifting algorithm in regularizing the distribution for interior particles. For this example, κ is simply set to 0 as there is no free surface boundary. Besides, since our particle shifting algorithm is motivated by the Helmholtz free energy functional, we can also introduce surface tension effects by independently adjusting the value of κ , see Figure 9 for a demonstration.

5 ADDRESSING THE PARTICLE CLUMPING PROBLEM

There are two typical models to compute the pressure force under the SPH framework: the symmetric repulsive pressure gradient model [6], [52], [54], [55] and the Taylor-series consistent pressure gradient model [1], [35]. The symmetric repulsive pressure gradient model has been widely used in SPH due to its superior stability features [33], [56]. However, this model is more sensitive to the tensile instability problem [8]. Therefore, we apply the Taylor-series consistent pressure gradient model to compute the pressure force as follows

$$\mathbf{F}_i^p = \frac{1}{\rho_0} \sum_j \left(\frac{1}{\hat{\alpha}_i} + \frac{1}{\hat{\alpha}_j} \right) (p_j - p_i) \mathbf{n}_{ij} \frac{\omega_{ij}}{r_{ij}}, \quad (33)$$

Next, we will discuss how to improve the Taylor-series consistent pressure gradient model to avoid pairing instability. Assume W is a kernel function that is commonly used in SPH. According to the Swegles condition of instability, a sufficient criterion for unstable growth in compressive regime is $W''(r) < 0$ (because the compressive stress is assumed to be negative in [12]), where W'' represents the second derivative of the kernel function. Invoking the relationship between ω and W in Equation 10, an equivalent sufficient criterion for unstable growth in terms of ω should be as follows

$$\Omega_\omega(r) = \frac{\omega}{r^2} - \frac{\omega'}{r} < 0. \quad (34)$$

That is say, in order to avoid pairing instability, it is better for us to select a kernel function satisfying $\Omega_\omega(r) > 0$.

Before proceeding with the choice of kernel function, it should be pointed out that Dehnen and Aly [15] disproved Swegles statement by showing that the Wendland functions (whose second derivative cannot be strictly larger than 0) can avoid the pairing instability for all scale of neighbors in WSPH. Unfortunately, as we apply the Wendland function (e.g., by setting $W(r) = (1 - \frac{r}{h})^3 (1 + 3\frac{r}{h})$ and $\omega(r) = -rW' = 12\frac{r^2}{h^2} (1 - \frac{r}{h})^2$) within our incompressible fluid solver, severe pairing instability is observed for a 2D dambreak test. Therefore, we still use Equation 34 as a guidance for selecting the appropriate kernel function. Since the sufficient criterion for unstable growth is now given in terms of ω , we actually have more freedom in selecting the kernel function, e.g., we can simply set ω rather than W to be a Wendland function. However, this also introduces another numerical problem involving the terms ω/r and ω/r^2 , since both the value of ω/r and ω/r^2 in Equation 8 could be extremely large when two neighboring particles

are too close to each other, resulting in simulation failure. To solve this problem, we propose to correct the kernel function as follows

$$\frac{\omega}{r} = \begin{cases} \frac{\omega(r)}{r}, & r > \delta \\ \frac{\omega(r)}{\delta}, & r \leq \delta \end{cases}, \quad \frac{\omega}{r^2} = \begin{cases} \frac{\omega(r)}{r^2}, & r > \delta \\ \frac{\omega(r)}{\delta^2}, & r \leq \delta \end{cases} \quad (35)$$

where δ is a threshold used to prevent ω/r and ω/r^2 from generating too large values. Unless stated, we will always set δ to be the particle sampling distance for all examples.

Motivated by the kernel function commonly used in MPS [57], we propose to use the following kernel function

$$\omega = \begin{cases} 1 - \frac{r^4}{h^4}, & r < h \\ 0, & r \geq h \end{cases}. \quad (36)$$

It can be easily verified $\Omega_\omega(t) > 0$ stands for all $r \in [0, h]$. To study its performance, Figure 10 tests two examples by selecting a set of different kernel functions. The rotating square patch is commonly used as a benchmark test for evaluation of numerical schemes in suppression of tensile instability while the dambreak is used for evaluation of pairing instability. In order to quantify simulation outcomes, we compute an average of the minimum distance of each particle to its neighbors as

$$\bar{d} = \frac{1}{N} \sum_i \min_{i \neq j} \|\mathbf{x}_i - \mathbf{x}_j\|. \quad (37)$$

Figure 11 plots the time history of \bar{d} for all dambreak simulations. From the comparison, it can be noticed both the Cubic and Wendland functions perform best in avoiding the pairing instability. However, in testing the rotation square example, simulations with the Cubic and Wendland functions break up much earlier than the one with our kernel function, which indicates our kernel function is better in suppressing the tensile instability. Since this work is focused on creating viscous fingering structures in fluids, we will always select Equation 36 as the kernel function in the following discussions. However, if researchers are interested in simulating examples mainly under compressive stress states, we suggest to use the Cubic or Wendland functions.

Till now, the last problem that has not been addressed is how to integrate all boundary conditions when calculating the pressure force. By invoking the free surface boundary condition $p_{js} = 0$, solid wall boundary condition defined in Equation 13 and the condition in Equation 20, we can reformulate the pressure force according to different types of fluid particles

$$\mathbf{F}_i^p = \frac{\beta_0}{\rho_0} \begin{cases} \sum_{j^b} \left(\frac{1}{\hat{\alpha}_i} + \frac{1}{\hat{\alpha}_j} \right) p_j \mathbf{n}_{ij} \frac{\omega_{ij}}{r_{ij}}, & i \in P^a \\ \sum_{j^b} \left(\frac{1}{\hat{\alpha}_i} + \frac{1}{\hat{\alpha}_j} \right) (p_j - p_i) \mathbf{n}_{ij} \frac{\omega_{ij}}{r_{ij}}, & i \in P^b \\ \sum_{j^b} \left(\frac{1}{\hat{\alpha}_i} + \frac{1}{\hat{\alpha}_j} \right) p_j \mathbf{n}_{ij} \frac{\omega_{ij}}{r_{ij}} + \Lambda_i^a + \Lambda_i^s, & i \in P^{a \wedge s} \\ \sum_{j^b} \left(\frac{1}{\hat{\alpha}_i} + \frac{1}{\hat{\alpha}_j} \right) (p_j - p_i) \mathbf{n}_{ij} \frac{\omega_{ij}}{r_{ij}} + \Lambda_i^s, & i \in P^s \end{cases} \quad (38)$$

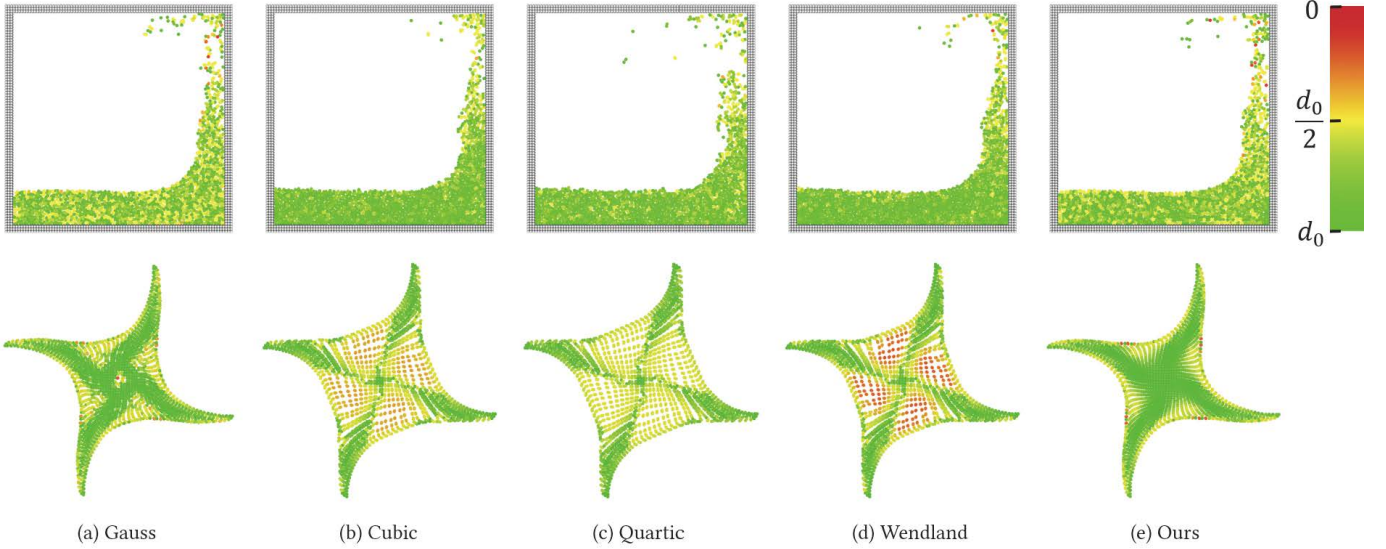


Fig. 10. Evaluation of the particle clumping problem with five different kernel functions. Top: A 2D dambreak is used for evaluation of numerical schemes in suppression of pairing instability; Bottom: A rotating square patch is used as a benchmark test for evaluation of numerical schemes in suppression of tensile instability.

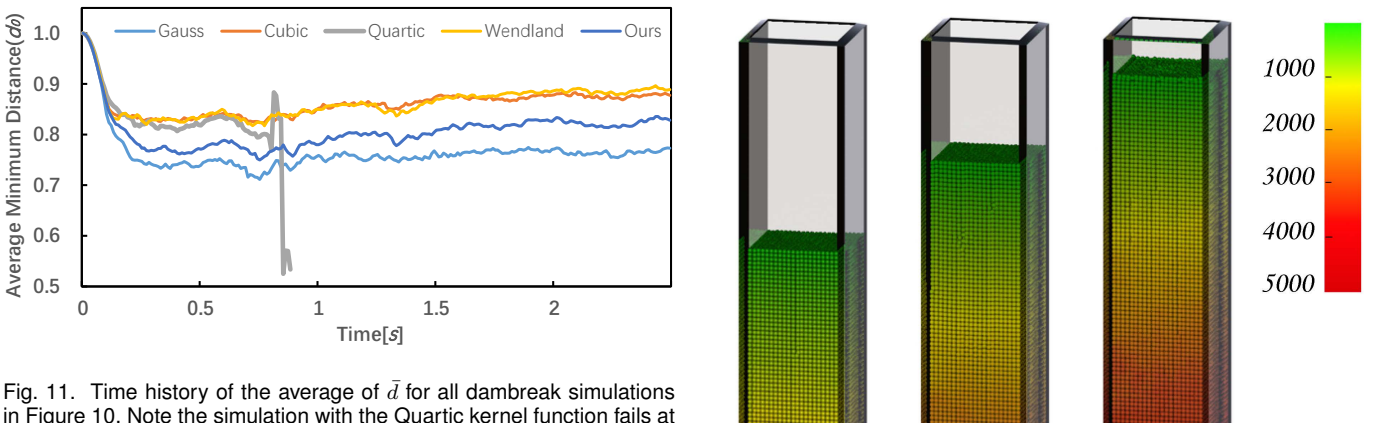


Fig. 11. Time history of the average of \bar{d} for all dambreak simulations in Figure 10. Note the simulation with the Quartic kernel function fails at around $t = 0.8$ s.

, where Λ_i^a and Λ_i^s are two sources originated from ghost air neighbors and ghost solid neighbors, respectively. Their formulations are written as

$$\Lambda_i^a = \sum_{j^b} \left(\frac{1}{\hat{\alpha}_i} + \frac{1}{\hat{\alpha}_j} \right) p_i \mathbf{n}_{ij} \frac{\omega_{ij}}{r_{ij}} \quad . \quad (39)$$

$$\Lambda_i^s = \sum_{j^s} \frac{2}{\hat{\alpha}_i} \text{proj}_{\mathbf{n}_{ij^s}} (\Delta \mathbf{v}_{ij^s}^*) \omega_{ij}$$

β_0 is a constant correction factor for the pressure force because the Taylor-series consistent pressure gradient model defined Equation 33 does not have a first-order accuracy. To reach a first-order accuracy, we first set β_0 to be 1 and initialize a linear pressure field, e.g., $p = x$, at the beginning of simulation. Then, we scale the value of β_0 to make the pressure force match its real value. The reason we do not apply a first-order Taylor-series pressure gradient model is because higher order models are more sensitive to the particle distribution, especially for boundary particles that suffer the particle deficiency problem [58].

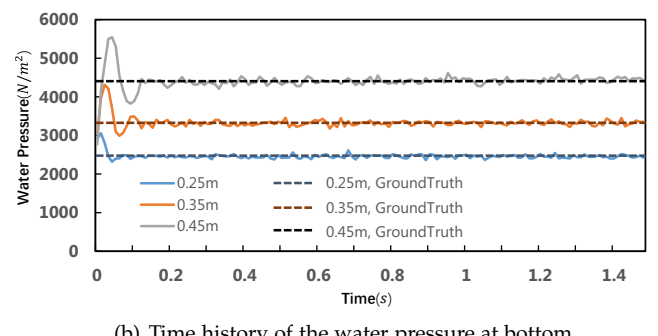


Fig. 12. Three hydrostatic water tests with different heights.

6 RESULTS AND DISCUSSIONS

We implement our method with CUDA and run all examples on an NVIDIA Geforce GTX 1060 graphics card. Algorithm 1 outlines an overview of our method. Before

Algorithm 1 Variational Staggered Incompressible SPH

```

1: Precompute  $A_0, \alpha_0, \beta_0, \nabla_0 c$  and  $\Delta_0 c$ ;
2: Initialize normal vectors for all ghost solid particles;
3: while  $t < t_{stop}$  do
4:    $\Delta t \leftarrow CFL(\mathbf{v}_i^t)$ ;
5:   for all fluid particle  $i$  do
6:      $\mathcal{N}_i \leftarrow$  Find neighbors;
7:     for all fluid particle  $i$  do
8:        $\mathbf{v}_i^* \leftarrow \mathbf{v}_i^t + \Delta t(\mathbf{F}^v + \mathbf{F}^{ext})$ ;
9:        $\mathbf{x}_i^* \leftarrow \mathbf{x}_i^t + \Delta t \mathbf{v}_i^*$ ;
10:    Run the particle shifting algorithm;
11:    for all fluid particle  $i$  do
12:      Compute  $A_i$  and  $\alpha_i$ ;
13:    Categorize fluid particles into four subsets;
14:    for all fluid particle  $i$  do
15:      Initialize the particle pressure  $p_i^0$ ;
16:      Compute  $\mathcal{L}_i^0$  according to Equation 14 and 19;
17:      Compute  $\mathcal{D}_i^0$  according to Equation 23;
18:      Compute the residual  $q_i^0 = \mathcal{L}_i^0 - \mathcal{D}_i^0$ ;
19:      Set  $y_i^0 = q_i^0$ ;
20:    Set the iteration number  $k = 0$ ;
21:    while  $\eta^k > \eta$  do
22:      for all fluid particle  $i$  do
23:        Compute  $\tilde{\mathcal{L}}_i^k$  in the same way as  $\mathcal{L}_i^k$  except  $p_i^k$  is replaced with  $y_i^k$ ;
24:        Compute  $\beta^k = \sum_i (q_i^k \cdot q_i^k) / \sum_i (y_i^k \cdot \tilde{\mathcal{L}}_i^k)$ ;
25:        for all fluid particle  $i$  do
26:          Update the pressure  $p_i^{k+1} = p_i^k + \beta^k r_i^k$ ;
27:          Update the residual  $q_i^{k+1} = q_i^k - \beta^k \tilde{\mathcal{L}}_i^k$ ;
28:        Compute  $\gamma^k = \sum_i (q_i^{k+1} \cdot q_i^{k+1}) / \sum_i (q_i^k \cdot q_i^k)$ ;
29:        for all fluid particle  $i$  do
30:          Update  $y_i^{k+1} = q_i^{k+1} + \gamma^k y_i^k$ ;
31:        for all fluid particle  $i$  do
32:          Compute  $\mathbf{F}_i^p$  according to Equation 38 with  $p_i^{k+1}$ ;
33:           $\mathbf{v}_i^{t+\Delta t} \leftarrow \mathbf{v}_i^* + \Delta t \mathbf{F}_i^p$ ;

```

the simulation starts, we precompute all reference values, including $A_0, \alpha_0, \beta_0, \nabla_0 c$ and $\Delta_0 c$, from a prototype particle with full neighbors. For each time step, we use a prediction-correction scheme similar to the two-step projection method [33], where the divergence-free condition $\nabla \cdot \mathbf{v} = 0$ is temporarily not fulfilled at the prediction step by advecting particles forward (lines 7~10) and is later imposed at the correction step by solving a pressure Poisson equation (lines 14~33). We compute an XSPH artificial viscous force \mathbf{F}^v following [42], [59] to stabilize inviscid flows. To avoid cumulative density errors, we additionally add an error compensating source (ECS) to the source term following Khayyer and Gotoh [60]. In our work, the error compensating source can be easily computed as follows

$$ECS_i^{t+\Delta t} = \left| \frac{\rho_i^t - \rho_0}{\rho_0} \right| \mathcal{D}_i^t + |\mathcal{D}_i^t| \left(\frac{\rho_i^t - \rho_0}{\rho_0} \right). \quad (40)$$

Please also note $ECS_i^{t+\Delta t}$ is only added to particles whose density ρ_i^t is larger than ρ_0 . If not specified, the smooth length h is always set to $h = 2.5d_0$. The time step size is limited by the Courant condition [33]. Surface meshes are

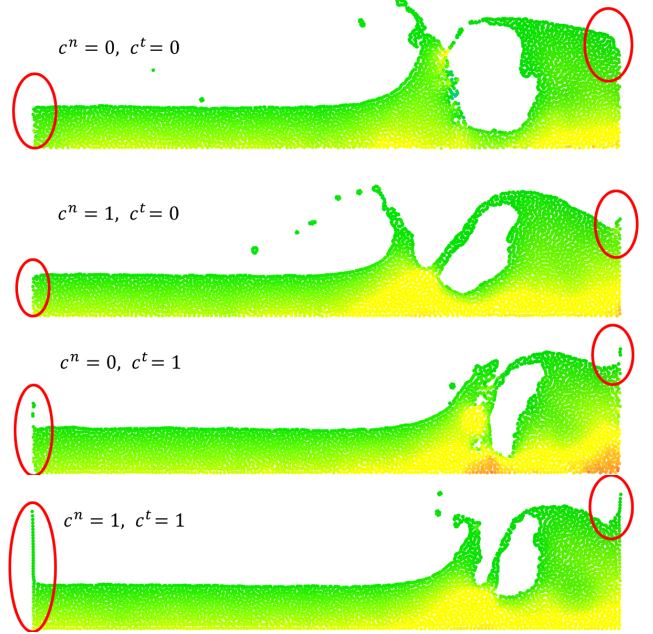


Fig. 13. A two-dimensional dambreak test with four different solid wall boundary conditions. Significant differences of flow patterns can be noticed near the solid wall.

reconstructed with the particle skinning method [61]. The open source code SPLisHSPlasH¹ has also been applied for the comparison in Figure 16.

Evaluation To evaluate the accuracy of our incompressible fluid solver, a benchmark test for hydrostatic water is performed. A set of pressure calculations with three different initial heights are carried out as shown in Figure 12(a), where the water density is set to 1000 kg/m^3 and the gravity is set to -9.8 m/s^2 . In the test, a no-slip solid wall boundary condition is imposed. The particle shifting algorithm is temporarily neglected so we can evaluate the accuracy of the incompressibility solver alone. Calculated pressure at the bottom of water shows that the simulation results converge to the analytical solution well, as shown in Figure 12(b). Besides, it can also be noticed from the video that the total volumes for all three tests are well preserved. In our second test, four different solid wall boundary conditions are imposed on a two-dimensional dambreak example. We can notice significant differences in the pressure fields and flow patterns near the solid wall boundary, as shown in Figure 13. Finally, Figure 6 compares the fluid patterns for different values of κ . In the case of $\kappa = 0$, the particle shifting algorithm is simply not performed. In other cases, it can be noticed that the particle shifting algorithm helps reduce pressure fluctuations caused by the irregularity of particle distributions. Besides, stronger surface tension effects are captured with a larger value of κ .

Comparison to staggered SPH [1] Figure 14 shows a comparison between our method and the staggered SPH method by dropping a liquid ball onto a table. To perform a fair comparison, we apply our particle shifting algorithm for both methods. Besides, we use the position-based method [5] to stabilize the simulation for staggered

1. <https://github.com/InteractiveComputerGraphics/SPLisHSPlasH>

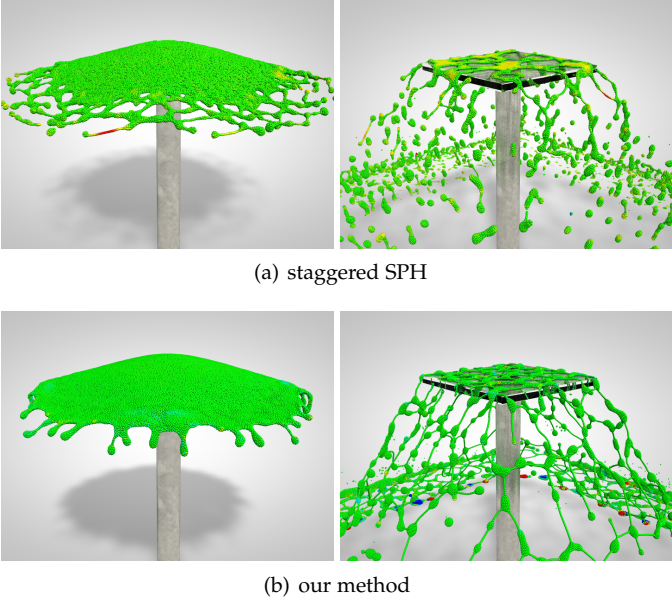


Fig. 14. A liquid ball onto a table. All other conditions for the comparison are the same except we use the position-based method [5], which is not necessary with our method, to stabilize the simulation for staggered SPH.

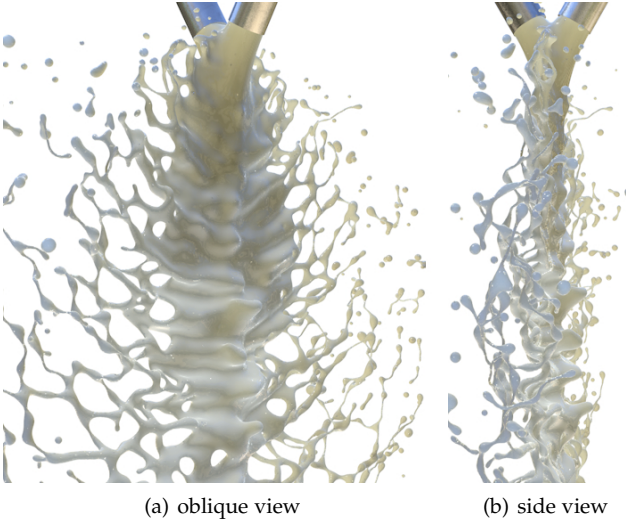


Fig. 15. High-velocity impinging jets with an inlet velocity of 24m/s . Impact waves arising from hydrodynamic instabilities are captured with our method.

SPH, which is not necessary with our method. It can be noted from the comparison that our method preserves thin features better than the staggered SPH method, especially for liquid jets and sheets. One reason could be due to the sensitiveness of staggered SPH in imposing free boundary conditions on particles. Another reason is that the Laplacian operator used in staggered SPH is quite similar to the one proposed by Cummins and Rudman [32], therefore, the same problem exists as analyzed in Section 3.2.

Liquid jets. Figure 16 shows two identical liquid jets impinging against each other, and a thin sheet resembling the shape of a fish bone forms around the intersection of the two jets. The flow patterns formed by the two liquid jets is extremely challenging for previous particle methods to

capture due to the particle deficiency and particle clumping problems. It portrays seven typical snapshots by different methods. To be fair in comparison, we only replace the incompressibility solver for the top three examples compared to the simulation in Figure 16(g), while keeping all other parts (including particle shifting, surface tension and viscosity) unchanged. Since both PCISPH and IISPH neglect the negative pressure, no thin liquid details can be captured. This also explains the importance of negative pressure forces in generating richer liquid details. DFSPH seems to be able to generate more details, however, no apparent viscous fingering structures can be noticed due to its low accuracy in solving the fluid incompressibility. To check how the dynamic behavior is affected by surface tension model, the bottom row compares three different surface tension models with other parts being solved in the same way as the simulation in Figure 16(g). To be fair, for each simulation, we tested more than five different surface tension coefficients and pick the best one in Figure 16(d), (e) and (f). Unfortunately, no previous surface tension model is able to create high-fidelity simulations of the formation and fragmentation of liquid sheets formed by two impinging jets. One reason could be because all three previous surface tension models are taken in an explicit manner, therefore the magnitude of surface tension force would be oscillatory and make the simulation results deteriorate. Finally, by taking a large inlet velocity, Figure 15 shows the impact waves arising from hydrodynamic instabilities can also be captured by our method. For more discussions on the impinging jets problem, we refer to the work by Chen et al. [62].

Milk crown. In Figure 17, we simulate a milk droplet that impacts on a milk body at 3m/s . Under the action of pressure force and surface tension, several thin jets are emitted around the rim that subsequently lead to the formation of the milk crown. Although the simulation result may still not comparable to those generated by the mesh-based methods [63], we believe our method have made a great breakthrough over previous particle methods in modeling the fingering structures. Figure 18 additionally demonstrates three milk droplets with different radii that impacts on a milk body. Different forms of the milk crown can be noticed due to the different size of milk droplets.

Performance. The linear system of equations is solved with a conjugate gradient method. By invoking the continuity equation for an ideal incompressible fluid, we have the following relationship that relates the residual of the linear system of equations to the density error

$$\eta = \frac{1}{N} \sum_i |\mathcal{L}_i - \mathcal{D}_i| = \frac{1}{\Delta t^2 N} \sum_i \frac{|\Delta \rho_i|}{\rho_0}, \quad (41)$$

where N is the total number of fluid particles. For a 2D dambreak case, Figure 19(a) shows several examples of the convergence of the conjugate gradient solver. It can be seen the residual error reduces by a factor of 10^6 at around 30 iterations. By requiring $|\Delta \rho| \leq 10^{-3} \rho_0$, we can set the convergence condition as $\eta_0 = 10^{-3}/\Delta t^2$, therefore only around 15 iterations are required.

To measure the convergence rate for the particle shifting

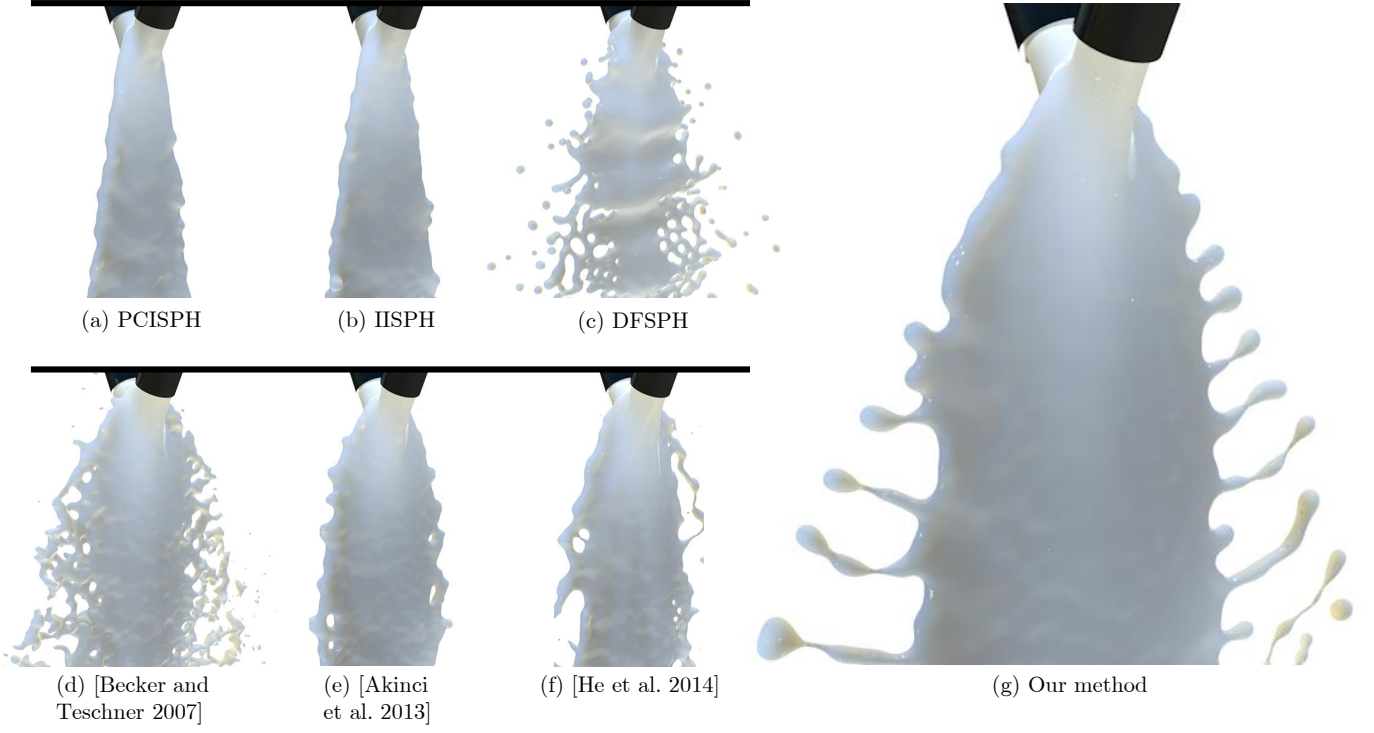


Fig. 16. Comparison of two impinging jets simulated with different incompressibility solvers and surface tension models, the inlet velocity is initialized to be 6.5m/s for all simulations.

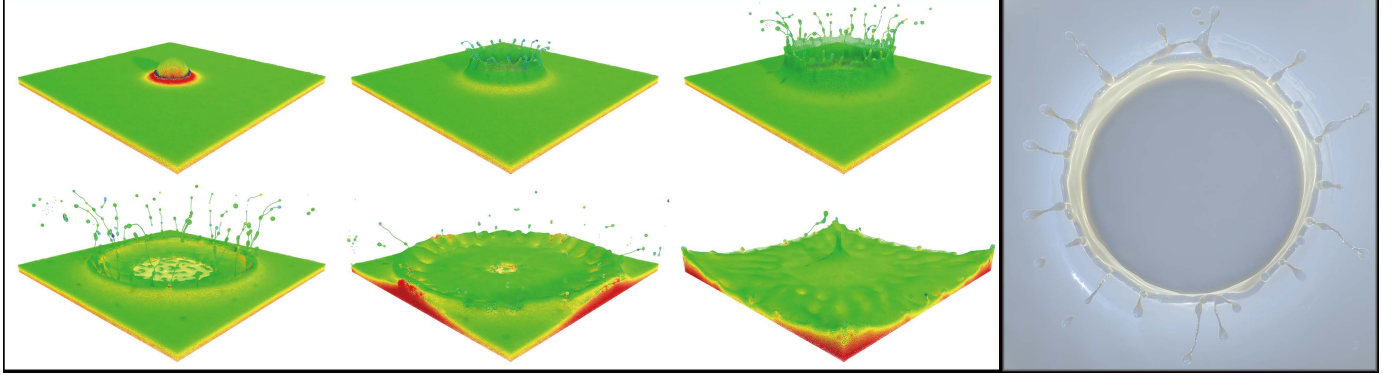


Fig. 17. Milk crown. This image shows the dynamic process of the formation and fragmentation of liquid jets and sheets, where particles are color-coded to demonstrate the pressure field.

algorithm, we define a metric as follows

$$\xi = \frac{1}{d_0 N} \sum_i \|\delta \mathbf{x}_i\| \quad (42)$$

Figure 19(b) shows the convergence of the particle shifting algorithm. It can be seen that the relative errors decrease rapidly at the first iterations. Therefore, we typically take a constant number of 10 iterations for the particle shifting algorithm. Table 1 shows other statistics and timings for all examples.

Limitations. Although the pressure force is corrected with β_0 , the accuracy of our method is still less than a first-order accuracy, especially when the particle distribution is irregular. Therefore, subtle fluctuations of the pressure field can be observed in solving the hydrostatic water test

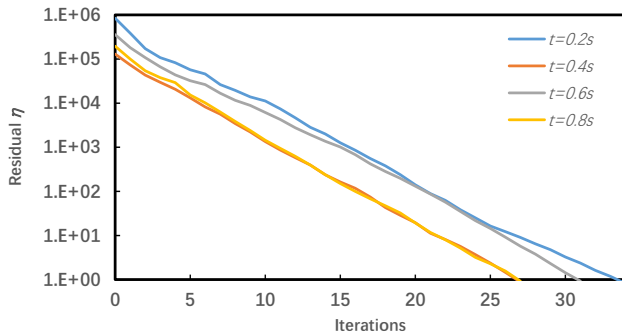
problem. Besides, a slight momentum loss exists because the Taylor-series consistent pressure gradient model dose not fully conserve the momentum. However, slightly losing a little momentum and kinetic energy is sometimes acceptable for computer graphics applications as long as it does not cause too much visual artifacts. Finally, some efforts on parameter tuning is required to capture plausible fingering structures, among which the most important parameters are the inlet velocity, the gradient energy coefficient κ and the viscosity coefficient.

7 CONCLUSIONS AND FUTURE WORK

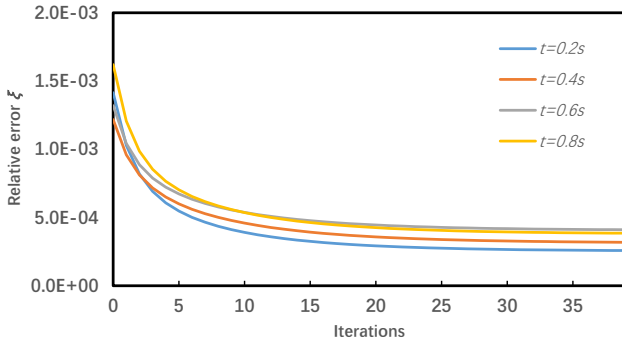
In this paper, we have introduced a novel approximate projection method under a variational staggered particle



Fig. 18. Three milk droplets of different radii impacting on a milk body at 3m/s . Under the combined action of pressure, surface tension and viscosity, thin jets are emitted around the rim that lead to the formation of milk crowns.



(a) Convergence examples of the conjugate gradient solver at different instants of time.



(b) Convergence examples of the particle shifting algorithm at different instants of time.

Fig. 19. Convergence statistics of the 2D dambreak example in Figure 9(b).

framework. After setting up the discretized pressure Poisson equation and categorizing all fluid particles into four subsets, we solve the particle deficiency problem by analytically imposing free-surface boundary conditions for both the Laplacian operator and the source term. Therefore, no ghost particles should be actually created during the simulation. In calculating the pressure force, we address the particle clumping problem by extending a Taylor-series consistent pressure gradient model with kernel correction. To regularize particle distributions, we introduce an iterative particle shifting algorithm motivated by Helmholtz free energy functional, which has the advantage of not only regularizing particle distributions, but also capturing plausible surface tension effects.

TABLE 1
Parameters and timings of all examples for one frame in average.

Name	size	c^n	c^t	κ	time/frame
Milk crown(Fig. 2)	1.2M	0.2	0.0	0.6	26s
3D dambreak(Fig. 6)	1.4M	0.2	0.0	0~0.1	1.2 min
Green vortex(Fig. 8)	2209	1.0	1.0	0.1	0.26s
2D dambreak(Fig. 9)	6589	0.2	0.0	0.1	0.48s
Liquid on table(Fig. 14)	113k	0.0	0.0	0.6	3.5s
Two jets(Fig. 16(g))	201k	-	-	0.3	4.0s
Three droplets(Fig. 18)	1.9M	0.2	0.0	0.6	1.7 min

For our future work, we will first consider how to conserve the total momentum with the Taylor-series consistent pressure gradient model. We will also investigate whether a higher order Laplacian [64] or a higher order source [65] can be integrated into our method to help improve the accuracy. Besides, it would be interesting to investigate how to solve the particle clumping and particle deficiency problems for an adaptive SPH solver [54], [66], [67]. Finally, we will consider extending our method to handle more complex scenarios involving two-way coupling between fluid and solid.

8 ACKNOWLEDGEMENT

The project was supported by the National Key R&D Program of China (No.2017YFB1002700), the National Natural Science Foundation of China (No.6187070657, 61632003), Youth Innovation Promotion Association, CAS (No.2019109) and Key Research Program of Frontier Sciences, CAS (No. QYZDY-SSW-JSC041).

REFERENCES

- [1] X. He, N. Liu, G. Wang, F. Zhang, S. Li, S. Shao, and H. Wang, "Staggered meshless solid-fluid coupling," *ACM Trans. Graph.*, vol. 31, no. 6, p. 149, 2012.
- [2] M. Becker and M. Teschner, "Weakly compressible SPH for free surface flows," in *Proceedings of SCA*, 2007, pp. 209–217.
- [3] B. Solenthaler and R. Pajarola, "Predictive-corrective incompressible SPH," *ACM Trans. Graph. (SIGGRAPH)*, vol. 28, no. 3, pp. 40:1–40:6, Jul. 2009.
- [4] X. He, N. Liu, S. Li, H. Wang, and G. Wang, "Local poisson SPH for viscous incompressible fluids," *Computer Graphics Forum*, vol. 31, no. 6, pp. 1948–1958, 2012.
- [5] M. Macklin and M. Müller, "Position based fluids," *ACM Trans. Graph. (SIGGRAPH)*, vol. 32, no. 4, p. 104, 2013.

- [6] M. Ihmsen, J. Cornelis, B. Solenthaler, C. Horvath, and M. Teschner, "Implicit incompressible SPH," *IEEE Transactions on Visualization and Computer Graphics*, vol. 20, no. 3, pp. 426–435, 2014.
- [7] J. Bender and D. Koschier, "Divergence-free smoothed particle hydrodynamics," in *Proceedings of SCA*. ACM, 2015, pp. 147–155.
- [8] H. Gotoh and A. Khayyer, "Current achievements and future perspectives for projection-based particle methods with applications in ocean engineering," *Journal of Ocean Engineering and Marine Energy*, vol. 2, no. 3, pp. 251–278, 2016.
- [9] H. Ikari, A. Khayyer, and H. Gotoh, "Corrected higher order laplacian for enhancement of pressure calculation by projection-based particle methods with applications in ocean engineering," *Journal of Ocean Engineering and Marine Energy*, vol. 1, no. 4, pp. 361–376, 2015.
- [10] A. Colagrossi, B. Bouscasse, M. Antuono, and S. Marrone, "Particle packing algorithm for SPH schemes," *Computer Physics Communications*, vol. 183, no. 8, pp. 1641–1653, 2012.
- [11] M. Liu and G. Liu, "Smoothed particle hydrodynamics (sph): an overview and recent developments," *Archives of Computational Methods in Engineering*, vol. 17, no. 1, pp. 25–76, 2010.
- [12] J. Sweigle, D. Hicks, and S. Attaway, "Smoothed particle hydrodynamics stability analysis," *Journal of computational physics*, vol. 116, no. 1, pp. 123–134, 1995.
- [13] J. J. Monaghan, "Sph without a tensile instability," *Journal of Computational Physics*, vol. 159, no. 2, pp. 290–311, 2000.
- [14] I. Schuessler and D. Schmitt, "Comments on smoothed particle hydrodynamics," *Astronomy and Astrophysics*, vol. 97, pp. 373–379, 1981.
- [15] W. Dehnen and H. Aly, "Improving convergence in smoothed particle hydrodynamics simulations without pairing instability," *Monthly Notices of the Royal Astronomical Society*, vol. 425, no. 2, pp. 1068–1082, 2012.
- [16] K. Sugiura and S.-i. Inutsuka, "An extension of godunov sph: Application to negative pressure media," *Journal of Computational Physics*, vol. 308, pp. 171–197, 2016.
- [17] X. He, H. Wang, F. Zhang, H. Wang, G. Wang, and K. Zhou, "Robust simulation of sparsely sampled thin features in SPH-based free surface flows," *ACM Trans. Graph.*, vol. 34, no. 1, pp. 7:1–7:9, Dec. 2014. [Online]. Available: <http://doi.acm.org/10.1145/2682630>
- [18] T. Belytschko and S. Xiao, "Stability analysis of particle methods with corrected derivatives," *Computers & Mathematics with Applications*, vol. 43, no. 3-5, pp. 329–350, 2002.
- [19] C. Batty, F. Bertails, and R. Bridson, "A fast variational framework for accurate solid-fluid coupling," *ACM Trans. Graph.*, vol. 26, no. 3, Jul. 2007. [Online]. Available: <http://doi.acm.org/10.1145/1276377.1276502>
- [20] Q. Du, M. Gunzburger, R. B. Lehoucq, and K. Zhou, "A nonlocal vector calculus, nonlocal volume-constrained problems, and non-local balance laws," *Mathematical Models and Methods in Applied Sciences*, vol. 23, no. 03, pp. 493–540, 2013.
- [21] G. C. Ganzenmüller, S. Hiermaier, and M. May, "On the similarity of meshless discretizations of peridynamics and smooth-particle hydrodynamics," *Computers & Structures*, vol. 150, pp. 71–78, 2015.
- [22] L. Lucy, "A numerical approach to the testing of the fission hypothesis," *The astronomical journal*, vol. 82, pp. 1013–1024, 1977.
- [23] R. Gingold and J. Monaghan, "Smoothed particle hydrodynamics-theory and application to non-spherical stars," *Monthly Notices of the Royal Astronomical Society*, vol. 181, pp. 375–389, 1977.
- [24] M. Desbrun and M.-P. Gascuel, *Smoothed particles: A new paradigm for animating highly deformable bodies*. Springer, 1996.
- [25] J. Monaghan, "Smoothed particle hydrodynamics," *Reports on Progress in Physics*, vol. 68, p. 1703, 2005.
- [26] M. Müller, D. Charypar, and M. Gross, "Particle-based fluid simulation for interactive applications," in *Proceedings of SCA*, 2003, pp. 154–159.
- [27] J. Monaghan, "Smoothed particle hydrodynamics," *Annual review of astronomy and astrophysics*, vol. 30, pp. 543–574, 1992.
- [28] K. Bodin, C. Lacouriere, and M. Servin, "Constraint fluids," *IEEE Transactions on Visualization and Computer Graphics*, vol. 18, no. 3, pp. 516–526, 2012.
- [29] M. Ihmsen, J. Orthmann, B. Solenthaler, A. Kolb, and M. Teschner, "Sph fluids in computer graphics," 2014.
- [30] D. Violeau and B. D. Rogers, "Smoothed particle hydrodynamics (sph) for free-surface flows: past, present and future," *Journal of Hydraulic Research*, vol. 54, no. 1, pp. 1–26, 2016.
- [31] J.-P. Fürstenau, B. Avci, and P. Wriggers, "A comparative numerical study of pressure-poisson-equation discretization strategies for sph," in *12th International SPHERIC Workshop, Ourense, Spain, June, 2017*, pp. 1–8.
- [32] S. J. Cummins and M. Rudman, "An SPH projection method," *Journal of computational physics*, vol. 152, no. 2, pp. 584–607, 1999.
- [33] S. Shao and E. Y. Lo, "Incompressible SPH method for simulating newtonian and non-newtonian flows with a free surface," *Advances in water resources*, vol. 26, no. 7, pp. 787–800, 2003.
- [34] P. Nair and G. Tomar, "An improved free surface modeling for incompressible sph," *Computers & Fluids*, vol. 102, pp. 304–314, 2014.
- [35] S. Yang, X. He, H. Wang, S. Li, G. Wang, E. Wu, and K. Zhou, "Enriching SPH simulation by approximate capillary waves," in *Proceedings of SCA*. Eurographics Association, 2016, pp. 29–36.
- [36] X. Hu and N. A. Adams, "A constant-density approach for incompressible multi-phase sph," *Journal of Computational Physics*, vol. 228, no. 6, pp. 2082–2091, 2009.
- [37] S. Band, C. Gissler, M. Ihmsen, J. Cornelis, A. Peer, and M. Teschner, "Pressure boundaries for implicit incompressible sph," *ACM Transactions on Graphics (TOG)*, vol. 37, no. 2, p. 14, 2018.
- [38] J. Cornelis, J. Bender, C. Gissler, M. Ihmsen, and M. Teschner, "An optimized source term formulation for incompressible sph," *The Visual Computer*, vol. 35, no. 4, pp. 579–590, 2019.
- [39] F. Losasso, J. Talton, N. Kwatra, and R. Fedkiw, "Two-way coupled SPH and particle level set fluid simulation," *IEEE Transactions on Visualization and Computer Graphics*, vol. 14, no. 4, pp. 797–804, 2008.
- [40] K. Raveendran, C. Wojtan, and G. Turk, "Hybrid smoothed particle hydrodynamics," in *Proceedings of SCA*. ACM, 2011, pp. 33–42.
- [41] Y. Zhu and R. Bridson, "Animating sand as a fluid," *ACM Trans. Graph. (SIGGRAPH)*, vol. 24, no. 3, pp. 965–972, Jul. 2005.
- [42] H. Schechter and R. Bridson, "Ghost SPH for animating water," *ACM Trans. Graph. (SIGGRAPH)*, vol. 31, no. 4, p. 61, 2012.
- [43] N. Tsuruta, A. Khayyer, and H. Gotoh, "A short note on dynamic stabilization of moving particle semi-implicit method," *Computers & Fluids*, vol. 82, pp. 158–164, 2013.
- [44] Q. W. Ma, Y. Zhou, and S. Yan, "A review on approaches to solving poisson's equation in projection-based meshless methods for modelling strongly nonlinear water waves," *Journal of Ocean Engineering and Marine Energy*, vol. 2, no. 3, pp. 279–299, Aug 2016. [Online]. Available: <https://doi.org/10.1007/s40722-016-0063-5>
- [45] R. Bridson, *Fluid simulation for computer graphics*. CRC Press, 2015.
- [46] R. Nestor, M. Basa, and N. Quinlan, "Moving boundary problems in the finite volume particle method," in *3rd ERCOFTAC SPHERIC Workshop on SPH Applications, Lausanne, Switzerland, June, 2008*, pp. 4–6.
- [47] R. Xu, P. Stansby, and D. Laurence, "Accuracy and stability in incompressible sph (isph) based on the projection method and a new approach," *Journal of computational Physics*, vol. 228, no. 18, pp. 6703–6725, 2009.
- [48] S. J. Lind, R. Xu, P. K. Stansby, and B. D. Rogers, "Incompressible smoothed particle hydrodynamics for free-surface flows: A generalised diffusion-based algorithm for stability and validations for impulsive flows and propagating waves," *Journal of Computational Physics*, vol. 231, no. 4, pp. 1499–1523, 2012.
- [49] A. Skillen, S. Lind, P. K. Stansby, and B. D. Rogers, "Incompressible smoothed particle hydrodynamics (sph) with reduced temporal noise and generalised fickian smoothing applied to body–water slam and efficient wave–body interaction," *Computer Methods in Applied Mechanics and Engineering*, vol. 265, pp. 163–173, 2013.
- [50] A. Khayyer, H. Gotoh, and Y. Shimizu, "Comparative study on accuracy and conservation properties of two particle regularization schemes and proposal of an optimized particle shifting scheme in isph context," *Journal of Computational Physics*, vol. 332, pp. 236–256, 2017.
- [51] J. Cahn and J. Hilliard, "Free energy of a nonuniform system. i. interfacial free energy," *The Journal of Chemical Physics*, vol. 28, p. 258, 1958.
- [52] T. Yang, J. Chang, B. Ren, M. C. Lin, J. J. Zhang, and S.-M. Hu, "Fast multiple-fluid simulation using helmholtz free energy," *ACM Transactions on Graphics (TOG)*, vol. 34, no. 6, p. 201, 2015.
- [53] S. Bouaziz, S. Martin, T. Liu, L. Kavan, and M. Pauly, "Projective dynamics: Fusing constraint projections for fast simulation," *ACM Trans. Graph. (SIGGRAPH)*, vol. 33, no. 4, pp. 154:1–154:11, 2014.

- [54] R. Winchenbach, H. Hochstetter, and A. Kolb, "Infinite continuous adaptivity for incompressible sph," *ACM Transactions on Graphics (TOG)*, vol. 36, no. 4, p. 102, 2017.
- [55] C. Gissler, A. Peer, S. Band, J. Bender, and M. Teschner, "Interlinked sph pressure solvers for strong fluid-rigid coupling," *ACM Trans. Graph.*, vol. 38, no. 1, pp. 5:1–5:13, Jan. 2019. [Online]. Available: <http://doi.acm.org/10.1145/3284980>
- [56] A. Khayyer, H. Gotoh, and S. Shao, "Corrected incompressible sph method for accurate water-surface tracking in breaking waves," *Coastal Engineering*, vol. 55, no. 3, pp. 236–250, 2008.
- [57] S. Koshizuka and Y. Oka, "Moving-particle semi-implicit method for fragmentation of incompressible fluid," *Nuclear science and engineering*, vol. 123, no. 3, pp. 421–434, 1996.
- [58] J. Fang, A. Parriaux, M. Rentschler, and C. Ancey, "Improved sph methods for simulating free surface flows of viscous fluids," *Applied Numerical Mathematics*, vol. 59, no. 2, pp. 251–271, 2009.
- [59] J. J. Monaghan, "On the problem of penetration in particle methods," *Journal of Computational Physics*, vol. 82, no. 1, pp. 1–15, May 1989.
- [60] A. Khayyer and H. Gotoh, "Enhancement of stability and accuracy of the moving particle semi-implicit method," *Journal of Computational Physics*, vol. 230, no. 8, pp. 3093–3118, 2011.
- [61] H. Bhattacharya, Y. Gao, and A. Bargteil, "A level-set method for skinning animated particle data," in *Proceedings of SCA*, 2011, pp. 17–24.
- [62] X. Chen, D. Ma, V. Yang, and S. Popinet, "High-fidelity simulations of impinging jet atomization," *Atomization and sprays*, vol. 23, no. 12, 2013.
- [63] N. Thürey, C. Wojtan, M. Gross, and G. Turk, "A multiscale approach to mesh-based surface tension flows," *ACM Trans. Graph. (SIGGRAPH)*, vol. 29, no. 4, pp. 48:1–48:10, Jul. 2010.
- [64] A. Khayyer and H. Gotoh, "A 3d higher order laplacian model for enhancement and stabilization of pressure calculation in 3d mps-based simulations," *Applied Ocean Research*, vol. 37, pp. 120–126, 2012.
- [65] ——, "Modified moving particle semi-implicit methods for the prediction of 2d wave impact pressure," *Coastal Engineering*, vol. 56, no. 4, pp. 419–440, 2009.
- [66] B. Adams, M. Pauly, R. Keiser, and L. J. Guibas, "Adaptively sampled particle fluids," *ACM Trans. Graph. (SIGGRAPH)*, vol. 26, no. 3, Jul. 2007.
- [67] B. Solenthaler and M. Gross, "Two-scale particle simulation," *ACM Trans. Graph. (SIGGRAPH)*, vol. 30, no. 4, pp. 81:1–81:8, Jul. 2011.